Chapter 11
A Short Review of Electromagnetic Force Models for Matter - Theory and Experimental Evidence

Wilhelm Rickert and Wolfgang H. Müller

Abstract From Maxwell's equations balance laws for the electromagnetic linear momentum, angular momentum, and energy can be found after recasting and using several identities of vector calculus. Therefore, the obtained equations are not "new results" but rather identities having the form of a balance law. However, there is some degree of freedom, (a) during construction of a particular identity and (b) for the choice of the to-be-balanced quantity, the non-convective flux, and the production term. In short, one is insecure which of the various forms is correct under which circumstances. This conundrum is referred to as the Abraham-Minkowski controversy, who first proposed different expressions for the electromagnetic linear momentum. The proper choice of electromagnetic force and torque expressions is of particular importance in matter where the mechanical and electromagnetic fields couple. The question arises as to whether a comparison between the predicted deformation behavior and the observed one can help to decide which electromagnetic force model is suitable for a material of interest. In this paper we shall briefly review the controversy and suggest new approaches for its solution on the continuum level.

Keywords: Electromagnetic force models · Magnetostriction · Electrostriction · Total forces and torques

11.1 Compilation of Relevant Force Models

Our starting point are the local balances of linear momentum for ponderable matter in regular points,

Wilhelm Rickert · Wolfgang H. Müller
Institut für Mechanik, Kontinuumsmechanik und Materialtheorie, Technische Universität Berlin, Sek. MS. 2, Einsteinufer 5, 10587 Berlin, Germany,
e-mail: rickert@tu-berlin.de, wolfgang.h.mueller@tu-berlin.de

H. Altenbach and A. Öchsner (eds.), *State of the Art and Future Trends in Material Modeling*, Advanced Structured Materials 100,
https://doi.org/10.1007/978-3-030-30355-6_11

$$\frac{\partial}{\partial t}(\rho \boldsymbol{v}) + \nabla \cdot (\rho \boldsymbol{v} \otimes \boldsymbol{v} - \boldsymbol{\sigma}) = \rho \boldsymbol{f} + \boldsymbol{f}^{\mathrm{EM}} , \tag{11.1}$$

and at a singular interface I with the normal $\boldsymbol{n}$ showing no intrinsic properties,

$$\boldsymbol{n} \cdot [\![\boldsymbol{\sigma} + \rho(\boldsymbol{w} - \boldsymbol{v}) \otimes \boldsymbol{v}]\!] = -\boldsymbol{f}_I^{\mathrm{EM}} , \tag{11.2}$$

where double brackets denote the jump across the interface. We denote by ρ the mass density, by $\boldsymbol{v}$ the particle velocity, by $\boldsymbol{w}$ the mapping velocity, by $\boldsymbol{f}$ the gravitational body force, and by $\boldsymbol{\sigma}$ the stress tensor. Unusual symbols worthy of a more detailed discussion are the volumetric electromagnetic force, $\boldsymbol{f}^{\mathrm{EM}}$, and its counterpart on a singular interface, $\boldsymbol{f}_I^{\mathrm{EM}}$. For these various expressions can be found in the literature, at least after some algebraic effort, and we will cite the pertinent references in what follows.

Probably the best known force model is the one attributed to Lorentz. We write:

$$\boldsymbol{f}^{\mathrm{L}} = q\boldsymbol{E} + \boldsymbol{J} \times \boldsymbol{B} , \qquad \boldsymbol{f}_I^{\mathrm{L}} = q_I \langle \boldsymbol{E} \rangle + \boldsymbol{J}_I \times \langle \boldsymbol{B} \rangle . \tag{11.3}$$

Pointed brackets refer to arithmetic averages of the right and left limit field values. q is the total charge, $\boldsymbol{J}$ is the total current, $\boldsymbol{E}$ and $\boldsymbol{B}$ are the electric and magnetic field vectors, respectively. The index I refers to the corresponding interface characteristics. All quantities are explained in detail for example in Müller (2014, Chapter 13). The correctness of these expressions is demonstrated indirectly in Müller (1985, Section 9.5) by construction of the standard Maxwell stress tensor and Poynting vector via Maxwell's equations. A more explicit proof is presented in Reich et al (2018, Appendix C). Suffice it to say that in the derivation and in those of the following force models ample use is made of the Maxwell-Lorentz-Aether relations, which hold true in an inertial system.

A second set of force models goes back to the work of Abraham (1909). Starting from the electromagnetic momentum density presented in that work and manipulating it similarly as the expression leading to the Lorentz force in Reich et al (2018) two different sets of expressions will result due to the intrinsic arbitrariness in the balance equations (see the example outlined in Reich et al, 2018, Section 2, for this issue):

$$\begin{aligned} \boldsymbol{f}^{\mathrm{A}_1} &= q\boldsymbol{E} + \boldsymbol{J} \times \mu_0 \mathfrak{H} + (\nabla \times \boldsymbol{B}) \times \boldsymbol{M} + \mu_0 \boldsymbol{D} \times \frac{\partial \boldsymbol{M}}{\partial t} , \\ \boldsymbol{f}_I^{\mathrm{A}_1} &= q_I \langle \boldsymbol{E} \rangle + \boldsymbol{J}_I \times \mu_0 \langle \mathfrak{H} \rangle - \mu_0 w_\perp \langle \boldsymbol{D} \rangle \times [\![\boldsymbol{M}]\!] + (\boldsymbol{n} \times [\![\boldsymbol{B}]\!]) \times \langle \boldsymbol{M} \rangle , \end{aligned} \tag{11.4}$$

and

$$\begin{aligned} \boldsymbol{f}^{\mathrm{A}_2} &= q\boldsymbol{E} + \boldsymbol{J} \times \mu_0 \mathfrak{H} - \nabla \cdot (\boldsymbol{M} \otimes \boldsymbol{B}) + \mu_0 \boldsymbol{D} \times \frac{\partial \boldsymbol{M}}{\partial t} , \\ \boldsymbol{f}_I^{\mathrm{A}_2} &= q_I \langle \boldsymbol{E} \rangle + \boldsymbol{J}_I \times \mu_0 \langle \mathfrak{H} \rangle - \mu_0 w_\perp \langle \boldsymbol{D} \rangle \times [\![\boldsymbol{M}]\!] + \\ &\quad + (\boldsymbol{n} \times [\![\boldsymbol{B}]\!]) \times \langle \boldsymbol{M} \rangle - \boldsymbol{n} \cdot [\langle \boldsymbol{M} \rangle \otimes [\![\boldsymbol{B}]\!] + [\![\boldsymbol{M}]\!] \otimes \langle \boldsymbol{B} \rangle] . \end{aligned} \tag{11.5}$$

We denote by $\mathfrak{H}$ the electric current potential in matter, by $\boldsymbol{M}$ the magnetization, $\boldsymbol{D}$ is the total charge potential, μ_0 is the vacuum permeability. Note that these two

choices are somewhat arbitrary and we could obtain even more force models from one electromagnetic momentum density.

In the same spirit the electromagnetic momentum density shown in the work by Minkowski (1910) leads to the following expressions:

$$\begin{aligned} \boldsymbol{f}^{\mathrm{M}_1} &= q\boldsymbol{E} + \boldsymbol{J}^{\mathrm{f}} \times \boldsymbol{B} + (\nabla \times \boldsymbol{M}) \times \boldsymbol{B} - (\nabla \times \boldsymbol{E}) \times \boldsymbol{P} \,, \\ \boldsymbol{f}_I^{\mathrm{M}_1} &= q_I \langle \boldsymbol{E} \rangle + \boldsymbol{J}_I^{\mathrm{f}} \times \langle \boldsymbol{B} \rangle + \langle \boldsymbol{P} \rangle \times (\boldsymbol{n} \times [\![\boldsymbol{E}]\!]) + (\boldsymbol{n} \times [\![\boldsymbol{M}]\!]) \times \langle \boldsymbol{B} \rangle \,, \end{aligned} \tag{11.6}$$

and

$$\begin{aligned} \boldsymbol{f}^{\mathrm{M}_2} &= q^{\mathrm{f}} \boldsymbol{E} + \boldsymbol{J}^{\mathrm{f}} \times \boldsymbol{B} - (\nabla \otimes \boldsymbol{M}) \cdot \boldsymbol{B} + (\nabla \otimes \boldsymbol{E}) \cdot \boldsymbol{P} \,, \\ \boldsymbol{f}_I^{\mathrm{M}_2} &= q_I^{\mathrm{f}} \langle \boldsymbol{E} \rangle + \boldsymbol{J}_I^{\mathrm{f}} \times \langle \boldsymbol{B} \rangle + \boldsymbol{n}(\langle \boldsymbol{P} \rangle \cdot [\![\boldsymbol{E}]\!] - \langle \boldsymbol{B} \rangle \cdot [\![\boldsymbol{M}]\!]) \,. \end{aligned} \tag{11.7}$$

$\boldsymbol{J}^{\mathrm{f}}$ and $\boldsymbol{J}_I^{\mathrm{f}}$ are the free total currents in regular and singular points, respectively, and q^{f} is the free charge density.

Finally, from the work of Einstein and Laub (1908) we find:

$$\begin{aligned} \boldsymbol{f}^{\mathrm{EL}} &= q^{\mathrm{f}} \boldsymbol{E} + \boldsymbol{J}^{\mathrm{f}} \times \mu_0 \mathfrak{H} + \boldsymbol{P} \cdot (\nabla \otimes \boldsymbol{E}) + \frac{\partial \boldsymbol{P}}{\partial t} \times \mu_0 \mathfrak{H} + \\ &\quad + \mu_0 \boldsymbol{M} \cdot (\nabla \otimes \mathfrak{H}) - \mu_0 \frac{\partial \boldsymbol{M}}{\partial t} \times \boldsymbol{D} \,, \\ \boldsymbol{f}_I^{\mathrm{EL}} &= \boldsymbol{f}_I^{\mathrm{M}_2} + \boldsymbol{n}[\![\boldsymbol{B} \cdot \boldsymbol{M} - \frac{\mu_0}{2} \boldsymbol{M} \cdot \boldsymbol{M}]\!] - w_\perp [\![\mathfrak{D} \times \mu_0 \boldsymbol{M} + \boldsymbol{P} \times \mu_0 \mathfrak{H}]\!] \,, \end{aligned} \tag{11.8}$$

where $\mathfrak{D}$ denotes the free charge potential.

11.2 Intermezzo

After the various force models have been presented the natural question arises as to which of them is the correct one? The answer is that all models are correct on the continuum scale for matter. There is not "the one" that will describe all situations correctly. Depending on the material one will be more realistic than the other. Experiments must decide which one this is. Various experiments come to mind. A first idea could be to measure the total force exerted on a body made of a material susceptible to external electromagnetic fields and to compare it with the total forces predicted by the various models. Second, it might be useful to study the deformation of that body. This requires us to solve a complex boundary value problem, because then we need to couple mechanics and electrodynamics, in particular we need to look at the stress-strain correlation. Third, besides forces it might be useful to study torques resulting during electromagnetic force interaction.

We shall outline the corresponding procedures in what follows in several case studies, which have been published by us before. Hence we just repeat the results, compare and comment on them. Our first example concerns a permanent magnetic, linear elastic sphere, resulting in magnetostriction. The second example is a silicone oil drop in castor oil (so that the oils do not mix) subjected to an external electric field.

Due to the different electric polarization in the two media deformation will result. The third example is the deformation of a spherical linear-elastic electret, similarly to magnetostriction, but with different types in poralization. And finally we shall report on the force and torque interaction between two rigid permanent spherical magnets.

11.3 Case I: Magnetostriction of a Spherical Permanent Magnet

This problem was analyzed before in detail in Reich et al (2018, Sect. 6). We considered the static case of a permanent magnetic sphere of radius R with uniform magnetization, $\boldsymbol{M} = M_0 \boldsymbol{e}_z$, which is treated as isotropically linear-elastic, with Lamé parameters λ and μ, mechanics-wise. In order to evaluate the expressions for the various force densities the following information for the electro-magnetic quantities are required:

$$\begin{aligned} &\boldsymbol{B}^{\mathrm{I}} = \tfrac{2}{3}\mu_0 \boldsymbol{M}\,, \quad \boldsymbol{\mathfrak{H}}^{\mathrm{I}} = -\frac{1}{3}\boldsymbol{M}\,, \quad q = q^{\mathrm{f}} - \nabla\cdot\boldsymbol{P} = 0\,, \\ &\boldsymbol{J} = \boldsymbol{J}^{\mathrm{f}} + \frac{\partial \boldsymbol{P}}{\partial t} + \nabla\times\boldsymbol{M} = \boldsymbol{0}\,, \quad q_{\scriptscriptstyle I} = q_{\scriptscriptstyle I}^{\mathrm{f}} - \boldsymbol{n}\cdot[\![\boldsymbol{P}]\!] = 0\,, \\ &\boldsymbol{J}_{\scriptscriptstyle I} = \boldsymbol{J}_{\scriptscriptstyle I}^{\mathrm{f}} - [\![\boldsymbol{P}]\!] w_\perp + \boldsymbol{n}\times[\![\boldsymbol{M}]\!] = \boldsymbol{n}\times[\![\boldsymbol{M}]\!]\,. \end{aligned} \tag{11.9}$$

Hence all of the volumetric force densities of all presented models vanish and the corresponding force densities on the interface are given by:

$$\begin{aligned} \boldsymbol{f}_{\scriptscriptstyle I}^{\mathrm{L}} &= \frac{1}{6}\mu_0 M_0^2(\sin^2\vartheta\,\boldsymbol{e}_r + 4\sin\vartheta\cos\vartheta\,\boldsymbol{e}_\vartheta) = \boldsymbol{f}_{\scriptscriptstyle I}^{(1)}\,, \\ \boldsymbol{f}_{\scriptscriptstyle I}^{\mathrm{A}_1} &= \frac{1}{6}\mu_0 M_0^2(\sin^2\vartheta\,\boldsymbol{e}_r + 4\sin\vartheta\cos\vartheta\,\boldsymbol{e}_\vartheta) = \boldsymbol{f}_{\scriptscriptstyle I}^{(1)}\,, \\ \boldsymbol{f}_{\scriptscriptstyle I}^{\mathrm{A}_2} &= \frac{1}{6}\mu_0 M_0^2(1 + 3\cos^2\vartheta)\boldsymbol{e}_r = \boldsymbol{f}_{\scriptscriptstyle I}^{(2)}\,, \\ \boldsymbol{f}_{\scriptscriptstyle I}^{\mathrm{M}_1} &= \frac{1}{6}\mu_0 M_0^2(\sin^2\vartheta\,\boldsymbol{e}_r + 4\sin\vartheta\cos\vartheta\,\boldsymbol{e}_\vartheta) = \boldsymbol{f}_{\scriptscriptstyle I}^{(1)}\,, \\ \boldsymbol{f}_{\scriptscriptstyle I}^{\mathrm{M}_2} &= \frac{1}{6}\mu_0 M_0^2(1 + 3\cos^2\vartheta)\boldsymbol{e}_r = \boldsymbol{f}_{\scriptscriptstyle I}^{(2)}\,, \\ \boldsymbol{f}_{\scriptscriptstyle I}^{\mathrm{EL}} &= \frac{1}{2}\mu_0 M_0^2\cos^2\vartheta\,\boldsymbol{e}_r = \boldsymbol{f}_{\scriptscriptstyle I}^{(3)}\,. \end{aligned} \tag{11.10}$$

It is noteworthy that in this case all models having (the same) symmetric electromagnetic stress measure (not shown here explicitly) yield the same surface force density. Interestingly, the non-symmetric Abraham and Minkowski models (also not detailed here) coincide for this magnetic problem. The Einstein-Laub model is distinct from the others. However, it can be seen that

$$\boldsymbol{f}_{\scriptscriptstyle I}^{\mathrm{EL}} = \boldsymbol{f}_{\scriptscriptstyle I}^{\mathrm{A}_2} - \frac{1}{6}\mu_0 M_0^2 \boldsymbol{e}_r,$$

hence these models differ only by a constant radial (pressure) offset. Qualitative representations of the surface force densities indicating the direction of deformation are shown in Fig. 11.1. The deformation field is now determined based on Hooke's law, mechanical equilibrium, and traction boundary conditions containing the various surface force densities. The method of Hiramatsu and Oka was applied for solving the resulting Lamé-Navier equations. It allows to obtain closed-form solutions in terms of Legendre polynomials. Sketches of the sphere deforming into different types of spheroids is shown in Fig. 11.2. Naively speaking one would now think that a simple measurement of the surface contour of an originally spherical object deforming after its magnetization would suffice to identify the "most realistic" surface force density. Unfortunately for a typical solid and reasonably high values of magnetization

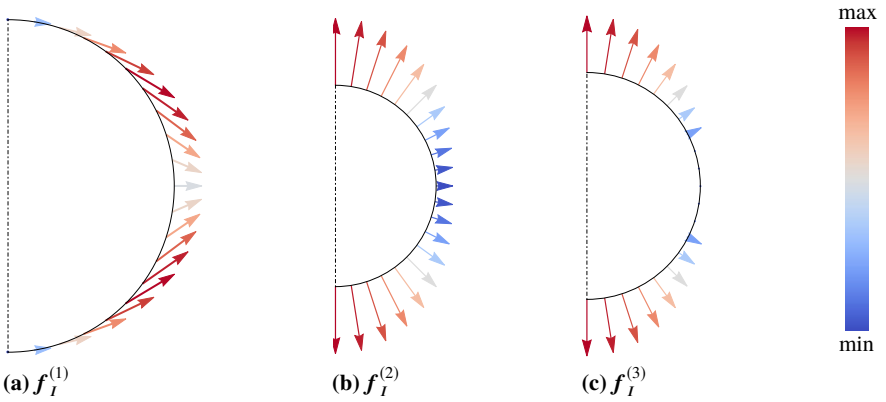

Fig. 11.1 Qualitative representations of the surface force densities. In (c), arrows are suppressed for small force magnitudes

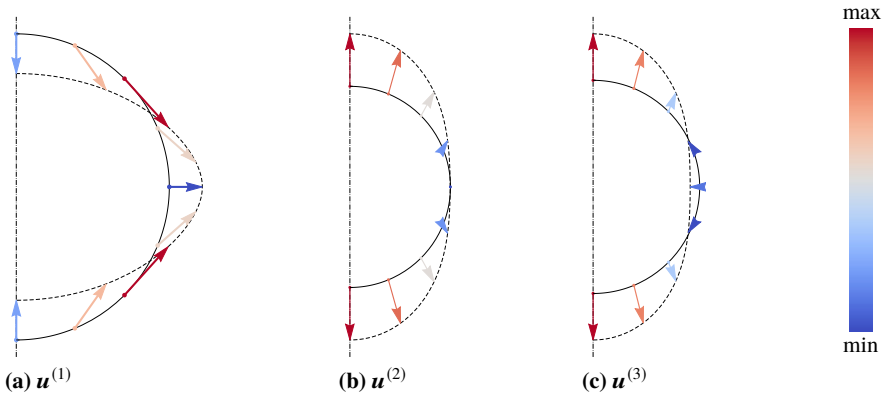

Fig. 11.2 Qualitative visualization of the surface displacements for the three electromagnetic force results. The ratio $\lambda/\mu = 1.27$ was used in order to model steel

the displacements are still extremely small (nanometer range), which renders a trustworthy measurement impossible. A more deformable object is required. Such a case will be presented in the next section.

11.4 Case II: Deformation of a Spherical Droplet due to Electric Polarization

This problem was analyzed before in detail in Reich et al (2018, Section 7). We considered the static case of a spherical silicone oil droplet of radius R in oxidized castor oil, placed in an homogeneous electric field $\boldsymbol{E}_0 = E_0 \boldsymbol{e}_z$. In fact there exists a real experiment for this case (Torza et al, 1971). Linear polarization laws with the relative dielectric constants of silicone oil $\epsilon_{\mathrm{r}}^{\mathrm{S}} \approx 2.8$ and of castor oil $\epsilon_{\mathrm{r}}^{\mathrm{C}} \approx 6.3$ were assumed, taken from the reference. Also, the densities of the oils are nearly equal. Hence, gravitational effects can be neglected.

As in the case of the magnetostriction the electro-magnetic field quantities were computed first. We found ($\mathcal{V}$ is proportional to the electric potential, indices S and C refer to the regions of the silicone drop and of the castor oil, respectively, $\tilde{r} = \frac{r}{R}$):

$$
\begin{aligned}
\boldsymbol{E} &= E_0(\boldsymbol{e}_z - \tilde{\nabla}\mathcal{V})\,, \quad [\![\mathcal{V}]\!] = 0\,,\\
\boldsymbol{P}^{\mathrm{S}} &= \epsilon_0(\epsilon_{\mathrm{r}}^{\mathrm{S}} - 1)\boldsymbol{E}^{\mathrm{S}} = E_0\epsilon_0(\epsilon_{\mathrm{r}}^{\mathrm{S}} - 1)(\boldsymbol{e}_z - \tilde{\nabla}\mathcal{V}^{\mathrm{S}})\,,\\
\boldsymbol{P}^{\mathrm{C}} &= \epsilon_0(\epsilon_{\mathrm{r}}^{\mathrm{C}} - 1)\boldsymbol{E}^{\mathrm{C}} = E_0\epsilon_0(\epsilon_{\mathrm{r}}^{\mathrm{C}} - 1)(\boldsymbol{e}_z - \tilde{\nabla}\mathcal{V}^{\mathrm{C}})\,,\\
\mathfrak{D}^{\mathrm{S}} &= \epsilon_0\epsilon_{\mathrm{r}}^{\mathrm{S}}\boldsymbol{E}^{\mathrm{S}} = E_0\epsilon_0\epsilon_{\mathrm{r}}^{\mathrm{S}}(\boldsymbol{e}_z - \tilde{\nabla}\mathcal{V}^{\mathrm{S}})\,,\\
\mathfrak{D}^{\mathrm{C}} &= \epsilon_0\epsilon_{\mathrm{r}}^{\mathrm{C}}\boldsymbol{E}^{\mathrm{C}} = E_0\epsilon_0\epsilon_{\mathrm{r}}^{\mathrm{C}}(\boldsymbol{e}_z - \tilde{\nabla}\mathcal{V}^{\mathrm{C}})\,,\\
\mathcal{V}^{\mathrm{S}} &= -\frac{\epsilon_{\mathrm{r}}^{\mathrm{C}} - \epsilon_{\mathrm{r}}^{\mathrm{S}}}{2\epsilon_{\mathrm{r}}^{\mathrm{C}} + \epsilon_{\mathrm{r}}^{\mathrm{S}}}\tilde{r}\cos\vartheta\,,\\
\mathcal{V}^{\mathrm{C}} &= -\frac{\epsilon_{\mathrm{r}}^{\mathrm{C}} - \epsilon_{\mathrm{r}}^{\mathrm{S}}}{2\epsilon_{\mathrm{r}}^{\mathrm{C}} + \epsilon_{\mathrm{r}}^{\mathrm{S}}}\tilde{r}^{-2}\cos\vartheta\,.
\end{aligned}
\tag{11.11}
$$

Similarly to the magnetostriction problem one finds that the volumetric force density vanishes for all the presented models. The surface densities are given by:

$$
\begin{aligned}
\boldsymbol{f}_I^{(4)} &= \boldsymbol{f}_I^{\mathrm{L}} = \boldsymbol{f}_I^{\mathrm{A}_1} = \boldsymbol{f}_I^{\mathrm{A}_2} = \boldsymbol{f}_I^{\mathrm{M}_1} = -(\boldsymbol{n}\cdot[\![\boldsymbol{P}]\!])\langle\boldsymbol{E}\rangle\\
&= -\frac{9}{2}\epsilon_0 E_0^2\frac{\epsilon_{\mathrm{r}}^{\mathrm{C}} - \epsilon_{\mathrm{r}}^{\mathrm{S}}}{(2\epsilon_{\mathrm{r}}^{\mathrm{C}} + \epsilon_{\mathrm{r}}^{\mathrm{S}})^2}[(\epsilon_{\mathrm{r}}^{\mathrm{C}} + \epsilon_{\mathrm{r}}^{\mathrm{S}})\cos^2\vartheta\boldsymbol{e}_r - 2\epsilon_{\mathrm{r}}^{\mathrm{C}}\cos\vartheta\sin\vartheta\boldsymbol{e}_\vartheta]\,,\\
\boldsymbol{f}_I^{(5)} &= \boldsymbol{f}_I^{\mathrm{M}_2} = \boldsymbol{f}_I^{\mathrm{EL}} = \boldsymbol{n}(\langle\boldsymbol{P}\rangle\cdot[\![\boldsymbol{E}]\!])\\
&= -\frac{9}{2}\epsilon_0 E_0^2\frac{\epsilon_{\mathrm{r}}^{\mathrm{C}} - \epsilon_{\mathrm{r}}^{\mathrm{S}}}{(2\epsilon_{\mathrm{r}}^{\mathrm{C}} + \epsilon_{\mathrm{r}}^{\mathrm{S}})^2}(2\epsilon_{\mathrm{r}}^{\mathrm{C}}\epsilon_{\mathrm{r}}^{\mathrm{S}} - \epsilon_{\mathrm{r}}^{\mathrm{C}} - \epsilon_{\mathrm{r}}^{\mathrm{S}})\cos^2\vartheta\boldsymbol{e}_r\,.
\end{aligned}
\tag{11.12}
$$

Sketches of the forces are depicted in Fig. 11.3. In order to compute the deformation

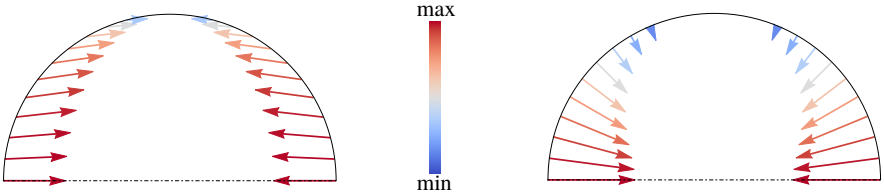

(a) Surface force $\boldsymbol{f}_I^{(4)}$. **(b)** Surface force $\boldsymbol{f}_I^{(5)}$.

Fig. 11.3 Qualitative representation of the computed force results for the oil drop experiment. For visualization, the values $\epsilon_{\mathrm{r}}^{\mathrm{S}} = 2.8$ and $\epsilon_{\mathrm{r}}^{\mathrm{C}} = 6.3$ were chosen. Note that the external electric field points in horizontal direction

the droplet was treated as a fluid at rest in terms of a hydrostatic pressure acting on it. A linear relationship between the pressure and the volume change was assumed and linked to the following (normalized) displacement *ansatz* on the interface

$$\boldsymbol{u}_I = \hat{u}(\tilde{u}_r(\vartheta)\boldsymbol{e}_r + \tilde{u}_\vartheta(\vartheta)\boldsymbol{e}_\vartheta) \,. \tag{11.13}$$

The deformation results of the experiments from Torza et al (1971) are depicted in Fig. 11.4c. For increasing electric field strength the drop deforms as an oblate spheroid. In Fig. 11.3 the surface force predictions of the various force models are qualitatively shown. $\boldsymbol{f}_I^{(4)}$ and $\boldsymbol{f}_I^{(5)}$ both suggest that the droplet should assume an oblate shape. Intuitively speaking, the surface force $\boldsymbol{f}_I^{(4)}$ might result in the correct deformation figure since the force $\boldsymbol{f}_I^5$ may cause dimples at poles, deviating from a spheroid form. Moreover, the magnitudes of the displacements differ. The models with the force $\boldsymbol{f}_I^{(4)}$ yields the smooth deformation figure depicted in Fig. 11.4a which is in good agreement with the experimental results in Fig. 11.4c. The deformation figure due to the models with the force $\boldsymbol{f}_I^{(5)}$ possesses a different curvature near the poles. Hence, the deformed body is not an oblate spheroid. However, this form is not observable in the experimental photographs. Therefore, it is reasonable to conclude that the models with the force $\boldsymbol{f}_I^{(5)}$ yield unphysical results, *i.e.*, the asymmetric Minkowski and the Einstein-Laub models are unlikely.

11.5 Case III: Elastic Deformation of Spherical Electrets due to Electric Polarization and Surface Charges

The analysis of this problem will be published in detail in Rickert et al (2019). Analogously to the droplet problem we shall consider the static case of spherical electrets. In (I), a linear dielectric in an externally applied electric field $\boldsymbol{E}_0$ is considered. Then, a real charge electret with surface charge $q_I^{\mathrm{f}} = Q/A_{\mathrm{sph}}$ is analyzed, (II). From these solutions the cases of an oriented dipole electret (III) and a real

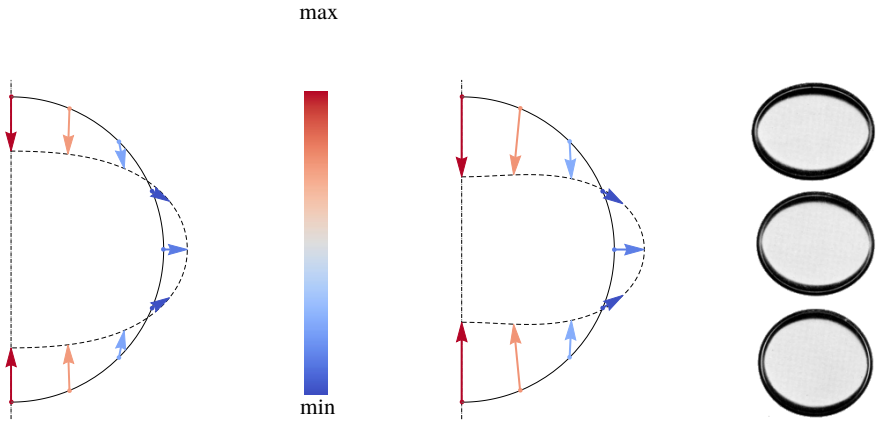

(a) Surface displacement $\boldsymbol{u}_I^{(4)}$.

(b) Surface displacement $\boldsymbol{u}_I^{(5)}$.

(c) Static case of (Torza et al, 1971, Fig. 7).

Fig. 11.4 Deformation figures of the oil droplet. (a) and (b): Predicted surface displacement using parameters $\epsilon_{\mathrm{r}}^{\mathrm{S}} = 2.8$, $\epsilon_{\mathrm{r}}^{\mathrm{C}} = 6.3$, $\gamma = 1$ and ${}^{\lambda_I}/_{\mu_I} = 1$. Scaling of the displacements was applied. (c): Experimental photos from Torza et al (1971, Fig. 7). The electric field points vertically. In (c), the electric field strength increases from the bottom to the top

charge electret with linear dielectric material behavior (IV) are readily obtained. We wish to calculate the various electromagnetic force densities and use them for predicting the deformation in situations (I)–(IV). As before the electromagnetic field quantities need to be determined first. By using the following scaling factors,

$$\frac{q_I^{\mathrm{f}}}{\epsilon_0} = \alpha\mathcal{E}\,,\ \frac{P_0}{\epsilon_0} = \beta\mathcal{E}\,,\ E_0 = \gamma\mathcal{E} \quad \Rightarrow\ a_0 = \frac{\alpha}{\epsilon_{\mathrm{r}}}\mathcal{E}\,,\ a_1 = \frac{\beta + (\epsilon_{\mathrm{r}} - 1)\gamma}{2\epsilon_{\mathrm{r}} + 1}\mathcal{E} \tag{11.14}$$

it can be shown that ($a_0 = \tilde{a}_0\mathcal{E}$, $a_1 = \tilde{a}_1\mathcal{E}$):

$$\begin{aligned}
\boldsymbol{E}^{\mathrm{I}} &= (\gamma - \tilde{a}_1)\mathcal{E}[\cos\vartheta\,\boldsymbol{e}_r - \sin\vartheta\,\boldsymbol{e}_\vartheta] = (\gamma - \tilde{a}_1)\mathcal{E}\boldsymbol{e}_z = \text{const.}\\
\boldsymbol{E}^{\mathrm{O}} &= \left\{\left[\tilde{a}_0\tilde{r}^{-2} + (2\tilde{a}_1\tilde{r}^{-3} + \gamma)\cos\vartheta\right]\boldsymbol{e}_r + \left(\tilde{a}_1\tilde{r}^{-3} - \gamma\right)\sin\vartheta\,\boldsymbol{e}_\vartheta\right\}\mathcal{E}\,,\\
\boldsymbol{P}^{\mathrm{I}} &= \kappa\epsilon_0\mathcal{E}[\cos\vartheta\,\boldsymbol{e}_r - \sin\vartheta\,\boldsymbol{e}_\vartheta] = \kappa\epsilon_0\mathcal{E}\boldsymbol{e}_z = \text{const.},\ \boldsymbol{P}^{\mathrm{O}} = \boldsymbol{0},\\
q_I &= \epsilon_0\left(\frac{q_I^{\mathrm{f}}}{\epsilon_0} - \boldsymbol{n}\cdot\frac{[\![\boldsymbol{P}]\!]}{\epsilon_0}\right) = \epsilon_0\mathcal{E}[\alpha + \kappa\cos\vartheta]\,,\\
\boldsymbol{J}_I &= -[\![\boldsymbol{P}]\!]w_\perp + \boldsymbol{n}\times[\![\boldsymbol{M}]\!] = \boldsymbol{0}\,,
\end{aligned} \tag{11.15}$$

where different scaling factors apply for the different situations:

$$
\begin{aligned}
&\text{(I)} && \mathcal{E} = E_0\,, && \alpha = 0\,, && \beta = 0\,, && \gamma = 1\,, && (\epsilon_\mathrm{r} \neq 1)\\
&\text{(II)} && \mathcal{E} = \frac{q_I^\mathrm{f}}{\epsilon_0}\,, && \alpha = 1\,, && \beta = 0\,, && \gamma = 0\,, && (\epsilon_\mathrm{r} = 1)\\
&\text{(III)} && \mathcal{E} = \frac{P_0}{\epsilon_0}\,, && \alpha = 0\,, && \beta = 1\,, && \gamma = 0\,, && (\epsilon_\mathrm{r} = 1)\\
&\text{(IV)} && \mathcal{E} = \frac{q_I^\mathrm{f}}{\epsilon_0}, && \alpha = 1\,, && \beta = 0\,, && \gamma = 0\,, && (\epsilon_\mathrm{r} \neq 1)
\end{aligned}
\tag{11.16}
$$

and $\kappa = \beta + (\gamma - \tilde{a}_1)(\epsilon_\mathrm{r} - 1)$. Now the non-vanishing surface force densities result:

$$
\begin{aligned}
\boldsymbol{f}_I^{(1)} &:= \boldsymbol{f}_I^{\mathrm{L}} = \boldsymbol{f}_I^{\mathrm{A}_1} = \boldsymbol{f}_I^{\mathrm{A}_2} = \boldsymbol{f}_I^{\mathrm{M}_1}\\
&= \epsilon_0 \mathcal{E}^2 \Bigg[\left(c_0^{(1)} \mathcal{P}_0(x) + c_1^{(1)} \mathcal{P}_1(x) + c_2^{(1)} \mathcal{P}_2(x) \right) \boldsymbol{e}_r +\\
&\quad + \left(d_1^{(1)} \frac{\mathrm{d}\mathcal{P}_1(x)}{\mathrm{d}\vartheta} + d_2^{(1)} \frac{\mathrm{d}\mathcal{P}_2(x)}{\mathrm{d}\vartheta} \right) \boldsymbol{e}_\vartheta \Bigg]\,,\\
\boldsymbol{f}_I^{(2)} &:= \boldsymbol{f}_I^{\mathrm{M}_2} = \boldsymbol{f}_I^{\mathrm{EL}}\\
&= \epsilon_0 \mathcal{E}^2 \left[\left(c_0^{(2)} \mathcal{P}_0(x) + c_1^{(2)} \mathcal{P}_1(x) + c_2^{(2)} \mathcal{P}_2(x) \right) \boldsymbol{e}_r + d_1^{(2)} \frac{\mathrm{d}\mathcal{P}_1(x)}{\mathrm{d}\vartheta} \boldsymbol{e}_\vartheta \right]\,.
\end{aligned}
\tag{11.17}
$$

$\mathcal{P}_i(x)$ denote Legendre polynomials and the coefficients are given by:

$$
\begin{aligned}
c_0^{(1)} &= \frac{1}{2}\alpha\tilde{a}_0 + \tfrac{1}{6}\kappa(\tilde{a}_1 + 2\gamma)\,, & c_1^{(1)} &= \frac{1}{2}\alpha(\tilde{a}_1 + 2\gamma) + \tfrac{1}{2}\kappa\tilde{a}_0\,,\\
d_1^{(1)} &= \alpha(\gamma - \tilde{a}_1)\,, & d_2^{(1)} &= \frac{1}{3}\kappa(\gamma - \tilde{a}_1)\,,\\
c_0^{(2)} &= \frac{1}{2}\alpha\tilde{a}_0 + \tfrac{1}{2}\kappa\tilde{a}_1\,, & c_1^{(2)} &= \frac{1}{2}\alpha(\tilde{a}_1 + 2\gamma) + \frac{1}{2}\kappa\tilde{a}_0\,,\\
c_2^{(1)} &= \frac{1}{3}\kappa(\tilde{a}_1 + 2\gamma)\,, & d_1^{(2)} &= \alpha(\gamma - \tilde{a}_1)\,, \quad c_2^{(2)} = \kappa\tilde{a}_1\,.
\end{aligned}
\tag{11.18}
$$

The various force densities are illustrated in Fig. 11.5. They may serve as first indication for the deformation pattern. Now in complete analogy to Case I the elastic deformation response can be calculated in closed form for (I)–(IV) as will be shown in Rickert et al (2019). The resulting forms are shown in Fig. 11.6.

Unfortunately, as in the case of magnetostriction, the displacements are very small making experimental investigations difficult.

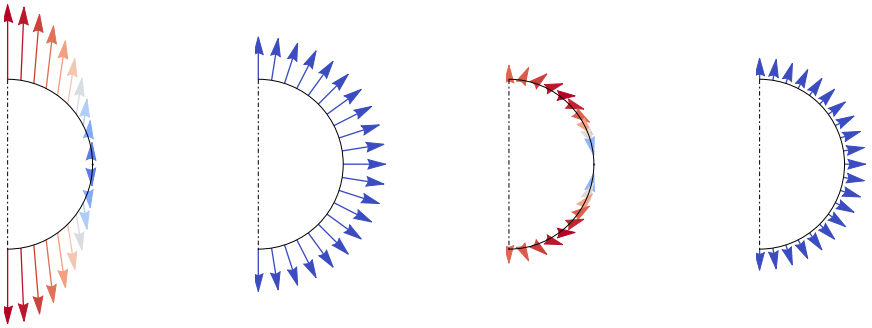

(a) $\boldsymbol{f}_I^{(1)}$ (I) **(b)** $\boldsymbol{f}_I^{(1)}$ (II) **(c)** $\boldsymbol{f}_I^{(1)}$ (III) **(d)** $\boldsymbol{f}_I^{(1)}$ (IV)

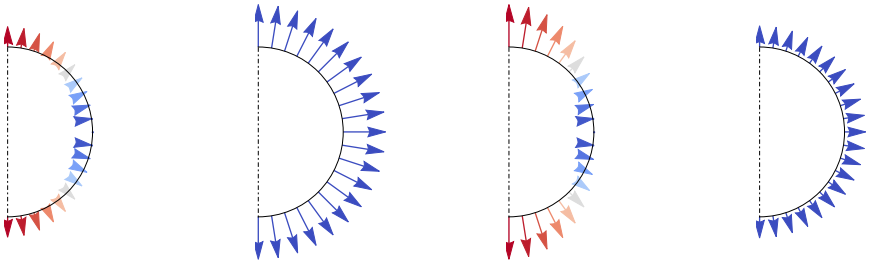

(e) $\boldsymbol{f}_I^{(2)}$ (I) **(f)** $\boldsymbol{f}_I^{(2)}$ (II) **(g)** $\boldsymbol{f}_I^{(2)}$ (III) **(h)** $\boldsymbol{f}_I^{(2)}$ (IV)

Fig. 11.5 Electret force densities predicted

11.6 Case IV: Force and Torque Interaction Between Spherical Magnets

The details of this problem will be published in Rickert and Müller (2019). We consider the interaction between two spherical rigid permanent magnets, homogeneously magnetized by $M_0^{(\mathrm{I})}$ and $M_0^{(\mathrm{II})}$ of radii $R_{(\mathrm{I})}$ and $R_{(\mathrm{II})}$, respectively: Fig. 11.7.

As one can show the dimensionless surface force densities $\tilde{\boldsymbol{f}}_I^{(\mathrm{EM})} = \boldsymbol{f}_I^{(\mathrm{EM})}/\hat{f}$ are given by:

$$\tilde{\boldsymbol{f}}_I^{\mathrm{L}} = \sin\vartheta' \boldsymbol{e}'_\varphi \times \tilde{\boldsymbol{B}}_{(\mathrm{I})} + \left\{ \frac{1}{6} \frac{M_0^{(\mathrm{II})}}{M_0^{(\mathrm{I})}} (\sin^2\vartheta' \boldsymbol{e}'_r + 4 \sin\vartheta' \cos\vartheta' \boldsymbol{e}'_\vartheta) \right\} ,$$

$$\tilde{\boldsymbol{f}}_I^{\mathrm{A}_1} = \sin\vartheta' \boldsymbol{e}'_\varphi \times \tilde{\boldsymbol{\mathfrak{H}}}_{(\mathrm{I})} + \left\{ \frac{1}{6} \sin\vartheta' \frac{M_0^{(\mathrm{II})}}{M_0^{(\mathrm{I})}} (\sin\vartheta' \boldsymbol{e}'_r + 4 \cos\vartheta' \boldsymbol{e}'_\vartheta) \right\} ,$$

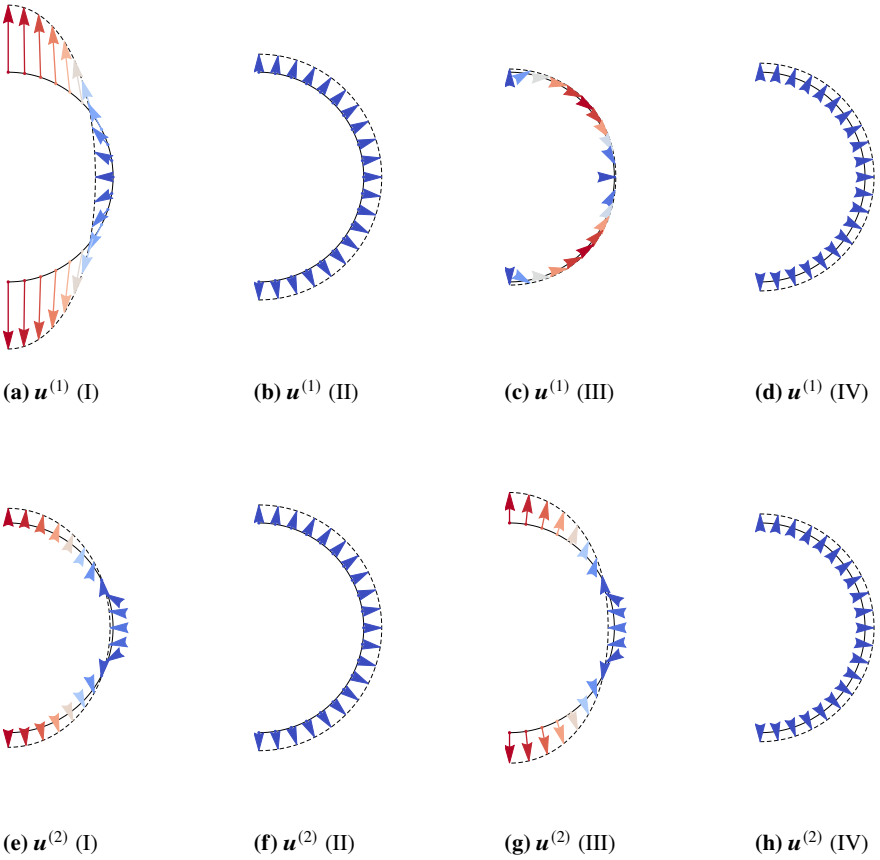

(a) $\boldsymbol{u}^{(1)}$ (I) **(b)** $\boldsymbol{u}^{(1)}$ (II) **(c)** $\boldsymbol{u}^{(1)}$ (III) **(d)** $\boldsymbol{u}^{(1)}$ (IV)

(e) $\boldsymbol{u}^{(2)}$ (I) **(f)** $\boldsymbol{u}^{(2)}$ (II) **(g)** $\boldsymbol{u}^{(2)}$ (III) **(h)** $\boldsymbol{u}^{(2)}$ (IV)

Fig. 11.6 Electret surface displacement predictions

$$\tilde{\boldsymbol{f}}_I^{\mathrm{A}_2} = \sin\vartheta' \boldsymbol{e}'_\varphi \times \tilde{\boldsymbol{\mathfrak{H}}}_{(\mathrm{I})} + \left\{ \cos\vartheta' \tilde{\boldsymbol{B}}_{(\mathrm{I})} + \frac{1}{6}\frac{M_0^{(\mathrm{II})}}{M_0^{(\mathrm{I})}}(1+3\cos^2\vartheta')\boldsymbol{e}'_r \right\} , \tag{11.19}$$

$$\tilde{\boldsymbol{f}}_I^{\mathrm{M}_1} = \sin\vartheta' \boldsymbol{e}'_\varphi \times \tilde{\boldsymbol{B}}_{(\mathrm{I})} + \left\{ \frac{1}{6}\frac{M_0^{(\mathrm{II})}}{M_0^{(\mathrm{I})}}(\sin^2\vartheta' \boldsymbol{e}'_r + 4\sin\vartheta'\cos\vartheta' \boldsymbol{e}'_\vartheta) \right\} ,$$

$$\tilde{\boldsymbol{f}}_I^{\mathrm{M}_2} = \boldsymbol{n}(\tilde{\boldsymbol{B}}_{(\mathrm{I})} \cdot \boldsymbol{e}'_z) + \left\{ \frac{1}{6}\frac{M_0^{(\mathrm{II})}}{M_0^{(\mathrm{I})}}(1+3\cos^2\vartheta')\boldsymbol{e}'_r \right\} ,$$

$$\tilde{\boldsymbol{f}}_I^{\mathrm{EL}} = \left\{ \frac{1}{6}\frac{M_0^{(\mathrm{II})}}{M_0^{(\mathrm{I})}}(1+3\cos^2\vartheta')\boldsymbol{e}'_r - \boldsymbol{n}\left(\frac{1}{2}\frac{M_0^{(\mathrm{II})}}{M_0^{(\mathrm{I})}}\sin^2\vartheta' + \frac{1}{6}\frac{M_0^{(\mathrm{II})}}{M_0^{(\mathrm{I})}}[4+3\cos^2\vartheta'] \right) \right\} ,$$

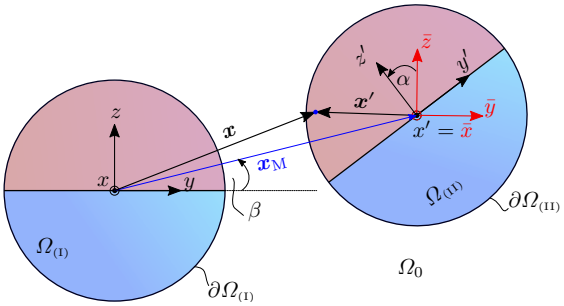

Fig. 11.7 Interacting spherical magnets

where $\hat{f} = \mu_0 M_0^{(\mathrm{I})} M_0^{(\mathrm{II})}$, $\boldsymbol{B}_{(\mathrm{I})} = \mu_0 M_0^{(\mathrm{I})} \tilde{\boldsymbol{B}}_{(\mathrm{I})}$ and $\mathfrak{H}_{(\mathrm{I})} = M_0^{(\mathrm{I})} \tilde{\mathfrak{H}}_{(\mathrm{I})}$. The expressions in curly brackets relate to the second magnet. The volumetric force densities normalized with $\hat{f} R_{(\mathrm{II})}^{-1}$ read:

$$\begin{aligned} \tilde{\boldsymbol{f}}^{\mathrm{L}} &= \tilde{\boldsymbol{f}}^{\mathrm{A}_1} = \tilde{\boldsymbol{f}}^{\mathrm{M}_1} = \tilde{\boldsymbol{f}}^{\mathrm{M}_2} = \boldsymbol{0}\,, \\ \tilde{\boldsymbol{f}}^{\mathrm{A}_2} &= -\tilde{\nabla} \cdot (\boldsymbol{e}_z' \otimes \tilde{\boldsymbol{B}}_{(\mathrm{I})})\,, \quad \tilde{\boldsymbol{f}}^{\mathrm{EL}} = \boldsymbol{e}_z' \cdot (\tilde{\nabla} \otimes \tilde{\mathfrak{H}}_{(\mathrm{I})})\,. \end{aligned} \tag{11.20}$$

In order to obtain the total force on the second magnet, the surface force densities are integrated across the surface of the second magnet and the volumetric forces across its volume. Then, the expressions in curly brackets do not contribute, as it should be. Moreover, as it can be shown with some effort (Rickert and Müller, 2019), the resulting forces are all equal independently of the model:

$$\boldsymbol{F}^{\mathrm{L}} = \boldsymbol{F}^{\mathrm{A}_1} = \boldsymbol{F}^{\mathrm{A}_2} = \boldsymbol{F}^{\mathrm{M}_1} = \boldsymbol{F}^{\mathrm{M}_2} = \boldsymbol{F}^{\mathrm{EL}}\,. \tag{11.21}$$

From the experimental point of view this is bad news because a measurement of the force would not allow us to identify the most realistic force density model. However, the situation is different when we consider the torque that magnet (I) imposes on magnet (II). The torque does depend on the model that is used. We find:

$$\begin{aligned} \boldsymbol{M}^{\mathrm{L}} &= \boldsymbol{M}^{\mathrm{A}_1} = \boldsymbol{M}^{\mathrm{M}_1} = \hat{f} R_{(\mathrm{II})}^3 \int\limits_{\partial\Omega_{(\mathrm{II})}} \sin\vartheta' \boldsymbol{e}_\varphi' (\boldsymbol{e}_r' \cdot \tilde{\boldsymbol{B}}_{(\mathrm{I})})\,\mathrm{d}\tilde{A}\,, \\ \boldsymbol{M}^{\mathrm{A}_2} &= -\hat{f} R_{(\mathrm{II})}^3 \int\limits_{\Omega_{(\mathrm{II})}} \boldsymbol{e}_r' \times \Big[\boldsymbol{e}_z' \cdot (\tilde{\nabla} \otimes \tilde{\boldsymbol{B}}_{(\mathrm{I})})\Big]\mathrm{d}\tilde{V} + \\ &\quad + \hat{f} R_{(\mathrm{II})}^3 \int\limits_{\partial\Omega_{(\mathrm{II})}} \boldsymbol{e}_r' \times \Big[(\sin\vartheta' \boldsymbol{e}_\varphi' \times \tilde{\mathfrak{H}}_{(\mathrm{I})} + \cos\vartheta' \tilde{\boldsymbol{B}}_{(\mathrm{I})})\Big]\mathrm{d}\tilde{A}\,, \\ \boldsymbol{M}^{\mathrm{M}_2} &= \hat{f} R_{(\mathrm{II})}^3 \int\limits_{\partial\Omega_{(\mathrm{II})}} \boldsymbol{e}_r' \times \Big[\boldsymbol{e}_r' (\tilde{\boldsymbol{B}}_{(\mathrm{I})} \cdot \boldsymbol{e}_z')\Big]\mathrm{d}\tilde{A} = \boldsymbol{0}\,, \\ \boldsymbol{M}^{\mathrm{EL}} &= \hat{f} R_{(\mathrm{II})}^3 \int\limits_{\Omega_{(\mathrm{II})}} \boldsymbol{e}_r' \times \Big[\boldsymbol{e}_z' \cdot (\tilde{\nabla} \otimes \tilde{\boldsymbol{B}}_{(\mathrm{I})})\Big]\mathrm{d}\tilde{V}. \end{aligned} \tag{11.22}$$

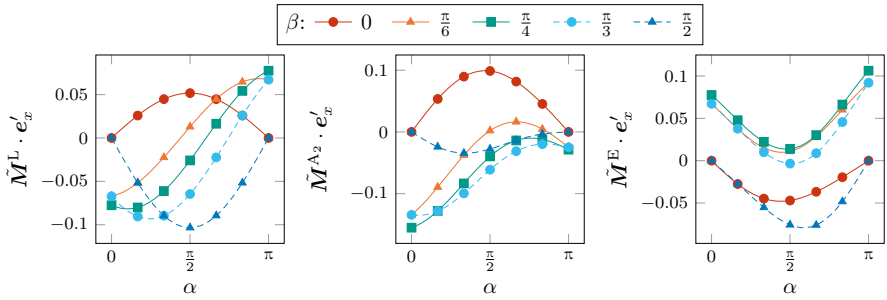

Fig. 11.8 Torques on the magnet (II) due to the magnetic field of the first one for different models and different configurations of the two magnets

Most interestingly, the second version of the Minkowski model yields no torque in any configuration of the two magnets. Therefore, we may conclude that this model is unrealistic. The non-vanishing torques are depicted in Fig. 11.8. From the figure it is clear, that the total torque on the second magnet is different for the distinct models and hence, only by measurement the correct force model for this situation can be found.

11.7 Conclusions and Outlook

The main objective of this paper was to draw attention to the fact that there exist different electromagnetic force models for ponderable matter. Which one is applicable depends on the concrete material that is subjected to electromagnetic fields. For a decision experiments must be performed and compared with theoretical predictions for the total force, the moment, and the deformation of the body in question. Four examples were presented to illustrate this complex situation. It is fair to say that in this context very few experiments have been performed and that the resulting deformations are usually very small, which makes a decision difficult. In conclusion one may say that until today the description of processes for bodies with a coupling between their thermo-mechanical and electromagnetic fields is still far from a complete rational understanding.

References

Abraham M (1909) Zur Elektrodynamik bewegter Körper. Rendiconti del Circolo Matematico di Palermo (1884-1940) 28(1):1–28

Einstein A, Laub J (1908) Über die im elektromagnetischen Felde auf ruhende Körper ausgeübten ponderomotorischen Kräfte. Annalen der Physik 331(8):541–550

Minkowski H (1910) Die Grundgleichungen für die elektromagnetischen Vorgänge in bewegten Körpern. Mathematische Annalen 68(4):472–525

Müller I (1985) Thermodynamics. Interaction of Mechanics and Mathematics Series, Pitman

Müller WH (2014) An Expedition to Continuum Theory. Springer, Dordrecht

Reich FA, Rickert W, Müller WH (2018) An investigation into electromagnetic force models: differences in global and local effects demonstrated by selected problems. Continuum Mechanics and Thermodynamics 30(2):233–266

Rickert W, Müller WH (2019) Dynamics of spherical magnets. Continuum Mechanics and Thermodynamics (in preparation)

Rickert W, Reich FA, Müller WH (2019) An examination of elastic deformation predictions of polarizable media due to various electromagnetic force models. Continuum Mechanics and Thermodynamics (in preparation)

Torza S, Cox RG, Mason SG (1971) Electrohydrodynamic deformation and burst of liquid drops. Philosophical Transactions of the Royal Society A: Mathematical, Physical and Engineering Sciences 269(1198):295–319